**Supplementary Information for**

# Eigenmode Steering in Spatiotemporal Gain–Loss Acoustic Metamaterials

Wai Chun Wong[1], Gregory J. Chaplain[1] and Jensen Li[1*]

[1]*Centre for Metamaterial Research and Innovation, Department of Physics and Astronomy, University of Exeter, United Kingdom*

## S.1 Proof of conservation of energy for cross-site nonlinear Hamiltonian

In this section, we describe a dimer system with added cross-coupled gain–loss coefficients and non-identical cavities. In this case, the nonlinear Hamiltonian in Eq. (2) in the main text becomes

$$H = \frac{1}{2}\begin{pmatrix} ig|\psi_b|^2/E & -\sqrt{\kappa_1\kappa_2}/2 \\ -\sqrt{\kappa_1\kappa_2}/2 & (\kappa_2' - \kappa_1')/2 - ig|\psi_a|^2/E \end{pmatrix}$$

where $\psi_a, \psi_b$ are the complex envelopes of the two cavities, $g$ control the cross-coupled gain–loss coefficient and $\kappa_1' = \sqrt{\omega_a/\omega_b}(-\delta + \kappa_1)$ and $\kappa_2' = \sqrt{\omega_b/\omega_a}(\delta + \kappa_2)$, are modified coupling coefficient, due to the detuning $\delta \cong \omega_b - \omega_a$ with $\kappa_1, \kappa_2$ the couplings between two cavities. When the cavities are identical, we have $\omega_a = \omega_b$, $\delta = 0$ and $\kappa_1 = \kappa_2 = \kappa$ which reduces to Eq. (2) in the main text.

To show the total energy $E = |\psi_a|^2 + |\psi_b|^2$ is conserved, we evaluate the energy change $dE/dt$. We express the change in total energy as:

$$\begin{aligned} \frac{dE}{dt} &= -i(\psi_a^* \quad \psi_b^*)(H - H^\dagger)\begin{pmatrix}\psi_a \\ \psi_b\end{pmatrix} \\ &= -\frac{i}{E}(\psi_a^* \quad \psi_b^*)\begin{pmatrix} ig|\psi_b|^2 & 0 \\ 0 & -ig|\psi_a|^2 \end{pmatrix}\begin{pmatrix}\psi_a \\ \psi_b\end{pmatrix} \\ &= 0 \end{aligned}$$

For three cavities, we first recall the nonlinear Hamiltonian in Eq. (5) in main text as

$$\begin{aligned} H &= H_3 + H_{NL} \\ &= \frac{1}{2}\begin{pmatrix} 0 & -\kappa/2 & -\kappa/2 \\ -\kappa/2 & 0 & -\kappa/2 \\ -\kappa/2 & -\kappa/2 & 0 \end{pmatrix} \\ &\quad + \frac{i}{2E}\begin{pmatrix} g_{ab}|\psi_b|^2 + g_{ac}|\psi_c|^2 & 0 & 0 \\ 0 & g_{bc}|\psi_c|^2 + g_{ba}|\psi_a|^2 & 0 \\ 0 & 0 & g_{ca}|\psi_c|^2 + g_{cb}|\psi_b|^2 \end{pmatrix} \end{aligned}$$

Similar to the dimer system, the change in total energy is:

$$\begin{aligned} \frac{dE}{dt} &= -i(\psi_a^* \quad \psi_b^* \quad \psi_c^*)\left(H_3 + H_{NL} - H_3^\dagger - H_{NL}^\dagger\right)\begin{pmatrix}\psi_a \\ \psi_b \\ \psi_c\end{pmatrix} \\ &= \frac{1}{E}(\psi_a^* \quad \psi_b^* \quad \psi_c^*)\begin{pmatrix} g_{ab}|\psi_b|^2 + g_{ac}|\psi_c|^2 & 0 & 0 \\ 0 & g_{bc}|\psi_c|^2 + g_{ba}|\psi_a|^2 & 0 \\ 0 & 0 & g_{ca}|\psi_c|^2 + g_{cb}|\psi_b|^2 \end{pmatrix}\begin{pmatrix}\psi_a \\ \psi_b \\ \psi_c\end{pmatrix} \\ &= \frac{1}{E}\left((g_{ab} + g_{ba})|\psi_a|^2|\psi_b|^2 + (g_{bc} + g_{cb})|\psi_b|^2|\psi_c|^2 + (g_{ca} + g_{ac})|\psi_c|^2|\psi_a|^2\right) \\ &= 0 \end{aligned}$$

since $g_{ij} = g_i - g_j = -g_{ji}$ for any pair of cavities $i, j \in \{a, b, c\}$ where $i \neq j$. This confirms that energy is conserved after adding cross-site nonlinear terms for both 2-cavity and 3-cavity systems.

## S.2 Derivation of Hilbert transform as quadrature component and its approximation

To clarify the relationship between the acoustic pressure $p(t)$ and its slowly varying complex envelope $\psi(t)$, we begin by expressing the pressure as

$$p(t) = \frac{1}{2}[\psi(t)e^{-i\omega_0 t} + \psi^*(t)e^{i\omega_0 t}],$$

where $\omega_0$ is the resonance (carrier) frequency. Assuming $\psi(t)$ varies slowly compared with $\omega_0$, its spectral bandwidth is much narrower than the carrier frequency. The Fourier transform of $p(t)$ can then be written as

$$\tilde{p}(\omega) = \frac{1}{2}[\tilde{\psi}(\omega - \omega_0) + \tilde{\psi}^*(\omega + \omega_0)],$$

where the first term represents the positive-frequency component, and the second term represents the negative-frequency component.

By definition, the Fourier transform of the Hilbert transform $\mathbb{H}[p]$ is given by [1]

$$\mathcal{F}\big[\mathbb{H}[p]\big] = -i\,\mathrm{sign}\,(\omega)\,\tilde{p}(\omega),$$

so that

$$\mathcal{F}\big[\mathbb{H}[p]\big] = -\frac{i}{2}[\mathrm{sign}\,(\omega)\tilde{\psi}(\omega - \omega_0) + \mathrm{sign}\,(\omega)\tilde{\psi}^*(\omega + \omega_0)].$$

Under the narrowband approximation, only frequencies near $\omega = \pm\omega_0$ contribute significantly, allowing the substitution

$$\mathrm{sign}(\omega - \omega_0) = +1, \mathrm{sign}(\omega + \omega_0) = -1.$$

Thus,

$$\mathcal{F}\big[\mathbb{H}[p]\big] \approx -\frac{i}{2}[\tilde{\psi}(\omega - \omega_0) - \tilde{\psi}^*(\omega + \omega_0)].$$

Taking the inverse Fourier transform gives

$$\mathbb{H}[p](t) = -\frac{i}{2}[\psi(t)e^{-i\omega_0 t} - \psi^*(t)e^{i\omega_0 t}].$$

Combining the above expressions for $p(t)$and $\mathbb{H}[p](t)$ yields

$$\psi(t)e^{-i\omega_0 t} = p(t) + i\,\mathbb{H}[p](t),$$

which completes our proof. If $\psi(t)$ is sufficiently slow varying, integration of $p(t)$ gives

$$\int p(t)\,dt \approx \frac{i}{2\omega_0}[\psi(t)e^{-i\omega_0 t} - \psi^*(t)e^{i\omega_0 t}] = -\frac{\mathbb{H}[p](t)}{\omega_0}.$$

This approximation is employed in the full-wave simulations to extract the quadrature component from the real-valued pressure field.

## S.3 Detailed system description for numerical simulation using Finite Element Method (FEM) and a more realistic implementation.

The geometry of the 3D coupled Helmholtz resonators is shown in Fig. S1. For the three-cavity case, three cavities and their connecting bridges are identical to the two-cavity case. To construct a bridge between cavities a and c, we divide the bridge into two halves and apply a continuity boundary condition at the end to connect them. Throughout the simulation, all boundaries are set to be sound-hard (rigid) unless otherwise specified.

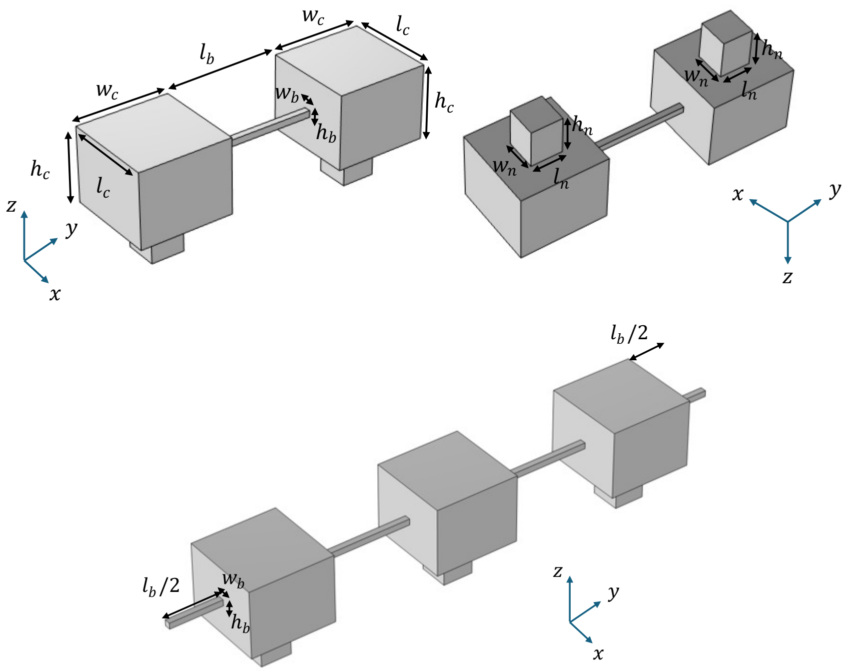


Figure S1 3D schematic of the coupled Helmholtz resonator geometry.

The model parameters, such as the resonance (carrier) frequency $\omega_0$ and the inter-resonator coupling coefficient $\kappa$ are related to the cavity, neck, and bridge geometries with approximated analytic formulas:

$$\omega_0 = c_0\sqrt{\frac{w_n l_n}{h_n}\frac{1}{w_c l_c h_c}}, \qquad \kappa = 2\frac{w_b h_b}{l_b}\frac{h_n}{w_n l_n}\omega_0. \tag{S3.1}$$

Moreover, to have mode steering, the gain-loss parameter $g$ has to be larger than $\kappa$. By adopting the active wall boundary condition through $v = Rp$, we can further prove that $g \propto R\omega_0$ with the remaining proportionality factor depending on the geometry of the cavities but independent of a global spatial scaling factor. These results establish the mode steering function can be solely characterized using two dimensionless parameters: $\kappa/\omega_0$ and $g/\omega_0$.

With such background, the geometric parameters are now chosen to give the model $\omega_0$ and $\kappa$, firstly guided by the formulas, listed in the Table S1 in the column of configuration 1. We note that since the geometry are uniform along the $x$-direction ($l_c = w_n = w_b$), they are further reduced to an equivalent 2D simulation, which is what we use in the manuscript. Then we have pinned down the more accurate values using simulations (2D for this configuration 1) to implement accurately the model requirement in main text: $\omega_0 = 2\pi \times 800$ Hz, $\kappa = 2\pi \times 163$ Hz. These sizes are justified as they are easily compatible with 3D printing and operation in audible frequencies with significantly low intrinsic loss.

| | Configuration 1 (2D equivalence, main text) | Configuration 2 (3D case) |
|---|---|---|
| $w_c$ | 6.0 cm | 5.6 cm |
| $l_c$ | 6.0 cm | 5.6 cm |
| $h_c$ | 3.0 cm | 4.5 cm |
| $w_n$ | 6.0 cm | 2.0 cm |
| $l_n$ | 0.5 cm | 2.0 cm |
| $h_n$ | 1.0 cm | 2.5 cm |
| $w_b$ | 6.0 cm | 0.4 cm |
| $l_b$ | 5.0 cm | 7.0 cm |
| $h_b$ | 0.2 cm | 0.4 cm |
| $\omega_0$ (formula) | $2\pi \times 909$ Hz | $2\pi \times 581$ Hz |
| $\kappa$ (formula) | $2\pi \times 145$ Hz | $2\pi \times 16.6$ Hz |

Table S1 Summarize of the geometry parameters used in the main text (configuration 1) and more realistic implementation in this section. Their approximated resonance frequency $\omega_0$ and coupling strength from Eq. ($S3.1$) is also provided.

From the above discussion, to have mode steering, we need $g$ (e.g. $2\pi \times 218$Hz) larger than $\kappa$, to justify its value, we actually examine the ratio $g/\omega_0$ so that we can compare to existing strategies to have gain. In main text, $g/\omega_0$ is chosen to be 25% to accelerate convergence in mode steering. The gain introduced from active components (in terms of linewidth) typically reported in active acoustic metamaterials is generally in the range of $g/\omega_0 \approx 5\%–10\%$[2, 3].

To assess the physical feasibility of the nonlinear dynamics reported, we perform additional three-dimensional full-wave simulations using experimentally realistic gain and coupling strengths. Here, we explicitly test whether the key phenomena, i.e. eigenmode collapse and Rabi-like oscillations, persist when the gain and coupling are restricted to values compatible with practical active acoustic implementations. To this end, we repeat the scenarios corresponding to Figs. 1 and 2 of the main text using the same modulation protocols, but with substantially reduced gain and coupling parameters.

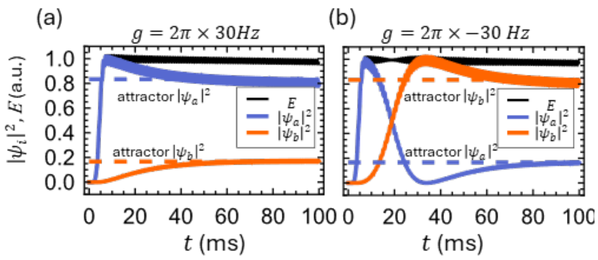


Figure S2 Simulated squared envelope amplitudes $|\psi_i|^2$ and total energy $E$ obtained from full three-dimensional simulations using experimentally realistic parameters. Panels (a, b) reproduce the dynamics shown in Fig. 1(d,e) of the main text, but with reduced gain and coupling strengths ( $g = \pm 2\pi \times 30$ Hz $\approx 0.06\,\omega_0$ , $\kappa = 2\pi \times 20$ Hz $\approx 0.04\,\omega_0$).

The geometric parameters are summarized in Table S1 as the configuration 2. For this configuration, the fundamental resonance frequency is $\omega_0 = 2\pi \times 518$ Hz, and the inter-cavity coupling strength is $\kappa = 2\pi \times 20$ Hz from 3D simulation. The active gain is implemented through the same feedback mechanism and is limited to a maximum value of $g = 2\pi \times 30$ Hz, corresponding to approximately 6% of the resonance frequency. These parameter values fall within experimentally realistic ranges for active acoustic systems.

Figure S2 shows the time evolution of the squared envelope amplitudes $|\psi_i|^2$ together with the total acoustic energy $E = |\psi_a|^2 + |\psi_b|^2$ obtained. These results correspond directly to the eigenmode-collapse scenario presented in Fig. 1(d,e) of the main text, but with the gain reduced to $g = 2\pi \times 30$ Hz ( $\sim 6\%$ of $\omega_0$ ). Despite the substantially lower gain, the system still converges to the same attractor eigenmode predicted by the effective Hamiltonian (dashed lines), demonstrating that the eigenmode collapse does not rely on unrealistically strong amplification. The primary effect of the reduced gain is an increased convergence time scale, consistent with the inverse dependence of the dynamics on the gain strength. Importantly, the total energy remains bounded throughout the evolution, confirming that the nonlinear feedback mechanism self-regulates the transient amplification and prevents runaway growth under experimentally realistic conditions.

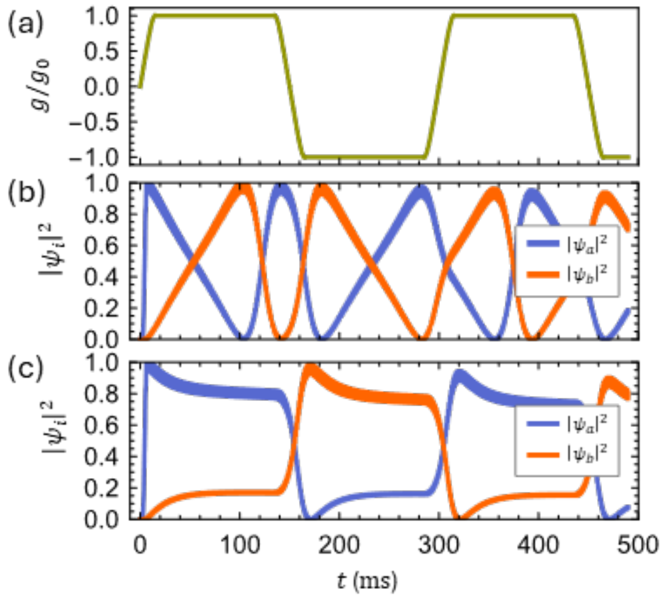


Figure S3 Time-dependent eigenmode steering with experimentally realistic gain parameters. (a) shows the temporal modulation of the gain parameter $g(t)$ , corresponding to the protocol used in Fig. 2(b) of the main text but with a rescaled time axis appropriate for reduced gain. Panels (b) and (c) show the resulting squared envelope amplitudes $|\psi_i|^2$ obtained from full three-dimensional simulations for modulation amplitudes $g_0 = 2\pi \times 15$ Hz and $g_0 = 2\pi \times 30$ Hz, respectively. In both cases, the system reproduces the same collapse–oscillation behavior reported in Fig. 2 of the main text, with reduced gain leading primarily to an increased characteristic time scale.

Figure S3 presents the time-dependent eigenmode-steering dynamics. These results correspond directly to the protocol shown in Fig. 2(b) of the main text, but with the gain reduced to $g_0 = 15$ Hz in Fig. S3 (b) and $g_0 = 30$ Hz in Fig. S3 (c) and the time axis rescaled accordingly. In both cases, the system reproduces the same qualitative collapse–oscillation behavior observed at higher gain: modulation within the $\mathcal{PT}$-symmetric regime in Fig. S3(b) produces sustained oscillations, whereas when the modulation drives the system into the $\mathcal{PT}$-broken regime in Fig. S3(c), the dynamics converge toward fixed-point eigenmodes. As in the eigenmode-collapse case, the primary effect of reducing the gain is an increase in the characteristic time scale, while the overall dynamical structure remains unchanged. Together with Fig. S2, these results demonstrate that both static and time-dependent eigenmode control persist under experimentally realistic conditions, confirming that the proposed steering mechanism is robust and not dependent on fine-tuned parameter choices.

For completeness we also describe the detailed simulation procedure. In this work, we first determine the cavity resonance frequency $\omega_0$ by a frequency domain simulation on the single cavity. We then simulate the coupled cavities to determine the coupling coefficient $\kappa$ for the two-cavity system. In the time-domain simulation, we input a pressure wave packet at the neck opening of the two cavities with a central frequency $\omega_0$ and a Gaussian envelope $e^{-t^2/\sigma^2}$, where $\sigma = 1/\omega_0$ . To obtain the gain–loss modulation, we first calculate $\left|\psi'_{a,b}\right|^2 = \left|p_{a,b} - i\omega_0 \int p_{a,b}\, dt\right|^2$ for the pressure signal $p_{a,b}$ on the top boundary of the two cavities. We then average along the top boundary to obtain $\left|\psi_{a,b}\right|^2 = \int \left|\psi'_{a,b}\right|^2 dl/w_c$. The nonlinear inter-site feedback is modeled through the time-varying acoustic wall parameter $R_{a,b}$ at the upper cavity walls, with $R_{a,b} = \mp k\, g\left|\psi_{b,\mathrm{a}}\right|^2/E$, where the total energy is $E = |\psi_a|^2 + |\psi_b|^2$ and the proportionality constant $k$ is fitted to the theoretical model and kept constant throughout this work for each configuration.

## S.4 Instantaneous eigenfrequency dynamics and stability of nonlinear system

In this section, we provide an eigenfrequency interpretation of the stability of the nonlinear dimer model used in the main text. Although the system is nonlinear and time-dependent, useful insight can be obtained by considering the instantaneous ("frozen-coefficient") spectrum of the effective Hamiltonian. The effective Hamiltonian can be written as

$$\mathrm{H(t) = H_{eff} - iG(t)I}$$

where

$$\mathrm{H_{eff}} = \frac{1}{2}\begin{pmatrix} \mathrm{ig}/2 & \kappa/2 \\ \kappa/2 & -\mathrm{ig}/2 \end{pmatrix}, \qquad G(t) = \frac{g}{4E}(|\psi_a(t)|^2 - |\psi_b(t)|^2).$$

In the $\mathcal{PT}$-broken phase ($g > \kappa$), the instantaneous eigenvalues are

$$\lambda_{\pm} = \pm\frac{i}{4}\sqrt{g^2-\kappa^2} - \mathrm{i}G$$

where the imaginary contribution from $H_{\text{eff}}$ corresponds to modal amplification. The instantaneous growth rate of the amplifying branch is therefore

$$\mathrm{Im}[\lambda_{\pm}] = \frac{1}{4}\sqrt{g^2-\kappa^2} + \frac{g}{4}(P_b - P_a)$$

where $P_{a,b} = \left|\psi_{a,b}\right|^2/E$ denote the normalized cavity energy fractions. Instantaneous amplification occurs only when this quantity is positive, yielding the condition

$$P_b - P_a > \pm\sqrt{1-(\kappa/g)^2}.$$

In the broken phase, mode steering drives the system toward the $\lambda_+$ branch, which possesses the larger imaginary part. At early times, when the energy is concentrated in cavity $b$, the imbalance satisfies $P_b - P_a > 0$, so both terms contributing to $\mathrm{Im}[\lambda_+]$ are positive, resulting in transient amplification. As the dynamics evolve, the state progressively aligns with the $\lambda_+$ eigenmode, whose associated eigenvector is

$$\{\psi_a, \psi_b\} = \left\{i\left(g+\sqrt{g^2-\kappa^2}\right), \kappa\right\},$$

The energy imbalance can then be evaluated by

$$P_b - P_a = \frac{\kappa^2 - \left(g+\sqrt{g^2-\kappa^2}\right)^2}{\kappa^2 + \left(g+\sqrt{g^2-\kappa^2}\right)^2} = -\sqrt{1-(\kappa/g)^2}$$

As the steering process proceeds, energy is transferred toward cavity $a$, and the energy imbalance decrease towards this value. Consequently, the term $(P_b - P_a)$ first becomes negative, and the nonlinear contribution to $\mathrm{Im}[\lambda_+]$ increasingly compensates the positive square-root term. When the system converge to this eigenmode, imbalance reaches a critical value such that the two terms balance, the imaginary part vanishes. Because $P_a$ and $P_b$ evolve dynamically, a slight overshoot can occur, as observed in Fig. 1(b,c) of the main text. In which the energy imbalance decrease further beyond this point, it becomes negative, resulting in damping. The system therefore relaxes toward a stable attractor, preventing unbounded energy growth.

## S.5 From non-Hermitian linear dynamics to nonlinear normalized evolution.

In this section we provide a detailed derivation showing that the nonlinear Hamiltonian used in the main text arises from a norm-preserving reformulation of a linear non-Hermitian two-level system. This establishes that the effective Hamiltonian description and the nonlinear Hamiltonian is deeply related. We begin with the linear evolution of an auxiliary (unnormalized) state $\{\phi_a, \phi_b\}$ governed by the non-Hermitian Hamiltonian

$$\frac{d}{dt}\begin{pmatrix}\phi_a\\ \phi_b\end{pmatrix} = H_{\text{eff}}\begin{pmatrix}\phi_a\\ \phi_b\end{pmatrix} = \frac{1}{2i}\begin{pmatrix} ig/2 & -\kappa/2\\ -\kappa/2 & -ig/2\end{pmatrix}\begin{pmatrix}\phi_a\\ \phi_b\end{pmatrix}. \qquad (S5.1)$$

Because the Hamiltonian is non-Hermitian, the norm $E_\phi = \sqrt{|\phi_a|^2 + |\phi_b|^2}$ is not conserved. A direct calculation yields

$$\frac{dE_\phi}{dt} = \frac{1}{2E_\phi}\frac{d}{dt}(|\phi_a|^2 + |\phi_b|^2) = \frac{g}{4E_\phi}(|\phi_a|^2 - |\phi_b|^2) \qquad (S5.2)$$

We now define a constant normalized state

$$\begin{pmatrix}\psi_a\\ \psi_b\end{pmatrix} = \frac{E_\psi}{E_\phi}\begin{pmatrix}\phi_a\\ \phi_b\end{pmatrix} \qquad (S5.3)$$

where $E_\psi$ is a constant normalization for $\psi$ state with the norm $E_\psi = \sqrt{|\psi_a|^2 + |\psi_b|^2}$.
Taking the time derivative of Eq. $(S5.3)$ and using Eq. $(S5.1)$, we obtain

$$\frac{d}{dt}\begin{pmatrix}\psi_a\\ \psi_b\end{pmatrix} = \frac{E_\psi}{E_\phi}\frac{d}{dt}\begin{pmatrix}\phi_a\\ \phi_b\end{pmatrix} - \frac{E_\psi}{E_\phi^2}\frac{dE_\phi}{dt}\begin{pmatrix}\phi_a\\ \phi_b\end{pmatrix} \qquad (S5.4)$$

Substituting Eqs. $(S5.1)$ and $(S5.2)$ into Eq. $(S5.4)$, we have

$$i\frac{d}{dt}\begin{pmatrix}\psi_a\\ \psi_b\end{pmatrix} = \frac{1}{2}\frac{E_\psi}{E_\phi}\begin{pmatrix} ig/2 & -\kappa/2\\ -\kappa/2 & -ig/2\end{pmatrix}\begin{pmatrix}\phi_a\\ \phi_b\end{pmatrix} - \frac{ig}{4}\frac{E_\psi}{E_\phi^3}(|\phi_a|^2 - |\phi_b|^2)\begin{pmatrix}\phi_a\\ \phi_b\end{pmatrix} \qquad (S5.5)$$

and expressing all quantities in terms of the normalized amplitudes $\psi_{a,b}$, we obtain

$$i\frac{d}{dt}\begin{pmatrix}\psi_a\\ \psi_b\end{pmatrix} = \frac{1}{2}\begin{pmatrix} ig/2 & -\kappa/2\\ -\kappa/2 & -ig/2\end{pmatrix}\begin{pmatrix}\psi_a\\ \psi_b\end{pmatrix} - \frac{ig}{4E_\psi^2}(|\psi_a|^2 - |\psi_b|^2)\begin{pmatrix}\psi_a\\ \psi_b\end{pmatrix} \qquad (S5.6)$$

Equation $(S5.5)$ is therefore identical to the Hamiltonian decomposition $H = H_{\text{eff}} - iGI$ introduced in the main text where $G = g/4E_\psi^2(|\psi_a|^2 - |\psi_b|^2)$. The Hamiltonian in Eq. (1), (2) in main text can then be obtained by combining two terms in $(S5.6)$.
This derivation shows that the nonlinear feedback appearing in the main text has a clear mathematical origin: it corresponds to subtracting the instantaneous mean growth rate of the non-Hermitian system in order to maintain a conserved norm. As a result, the effective gain at one site becomes proportional to the intensity at the opposite site, yielding the cross-coupled structure used throughout the manuscript.

## S.6 Latency consideration in realistic system

In our model, we assume that the acoustic pressure at the top cavity wall can be detected and converted into the corresponding analytic signal instantaneously. In a realistic implementation, however, digital signal processing introduces a finite latency $\tau$. Two main sources of delay arise from the Hilbert transform used to extract the analytic signal and a possible bandpass filter applied to the pressure signal to suppress unintended amplification. In this section, we investigate both effects by numerically simulating the system with explicit delays.

We first consider the delay associated with the Hilbert transform, which depends on the estimation method. For a narrowband signal, the Hilbert transform can be approximated by a discrete-time integrator of the form

$$y[n] - y[n-1] = p[n]T_s \tag{S6.1}$$

where $p[n]$ denotes the measured pressure, $T_s$ is the sampling period, and $y[n]$ provides a discrete approximation to $\int p(t)\, dt$. This discrete-time implementation introduces an effective group delay of approximately one-half sampling period. For a representative sampling frequency of 20 kHz, this corresponds to $\tau_{\text{as}} = 25$ us.

To assess the impact of this latency, we performed numerical simulations in which the nonlinear feedback terms are explicitly delayed by $\tau_{\text{as}}$. The Hamiltonian is modified as

$$H(t) = \frac{1}{2}\begin{pmatrix} ig|\psi_b(t-\tau_{\text{as}})|^2/E & -\kappa/2 \\ -\kappa/2 & -ig|\psi_a(t-\tau_{\text{as}})|^2/E \end{pmatrix} \tag{S6.2}$$

and the results are shown in Fig. S4. The delayed dynamics closely follow the ideal (no-delay) case, with only negligible quantitative differences and no change in the qualitative features of eigenmode collapse or mode steering.

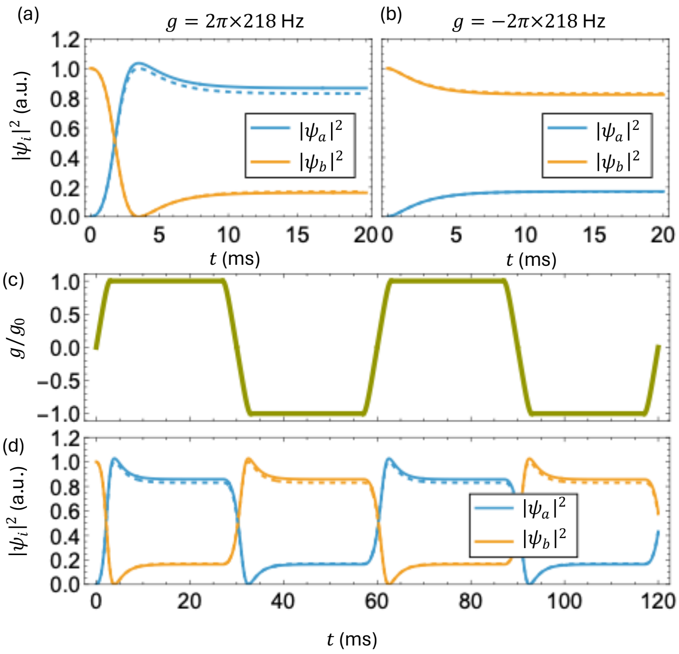


Fig. S4. Simulated nonlinear dynamics with an explicit delay $\tau_{\text{as}}$ in the nonlinear terms. The case without time delay $\tau_{\text{as}}$ is shown in dashed curves. (a) and (b) using the same gain parameters $g = \pm 2\pi \times 218$ Hz and $\kappa = 2\pi \times 168$ as in Fig. 1 (d) and (e) in main text. (d) shows the case with mode steering due to gain parameter shown in (c) with $g_0 = 2\pi \times 218$ Hz which is identical to the setting in Fig. 2 (c) in main text.

In practice, filtering is often introduced to stabilize the feedback loop, but it also contributes additional group delay depending on the filter design. To evaluate this effect, we perform finite-element simulations including a second-order bandpass filter applied to the pressure signal $p$, centered at the carrier frequency $\omega_0 = 2\pi \times 795$ Hz. The filtered signal $p_{\text{filt}}$ is express as:

$$\frac{d^2 p_{filt}}{dt^2} + \frac{\omega_0}{Q}\frac{dp_{filt}}{dt} + \omega_0^2 p_{filt} = \frac{\omega_0}{Q}\frac{dp}{dt} \qquad (S6.3)$$

where $Q = 1$ is chosen as a compromise between filter selectivity and delay. The filtered pressure is used to derive the complex envelope $\psi$ and the corresponding wall parameter $R$, and the acoustic velocity normal to the wall is given by $v = p_{\text{filt}}/R$.

The simulations shown in Fig. S5 repeat the configurations of Figs. 1(d,e) and 2(c) in the main text using identical gain parameters and cavity geometry. Although the additional delay introduced by the filter leads to increased overshoot and oscillations in the total energy, the mode-steering dynamics remain unchanged, demonstrating the robustness of the mechanism to realistic signal-processing delays.

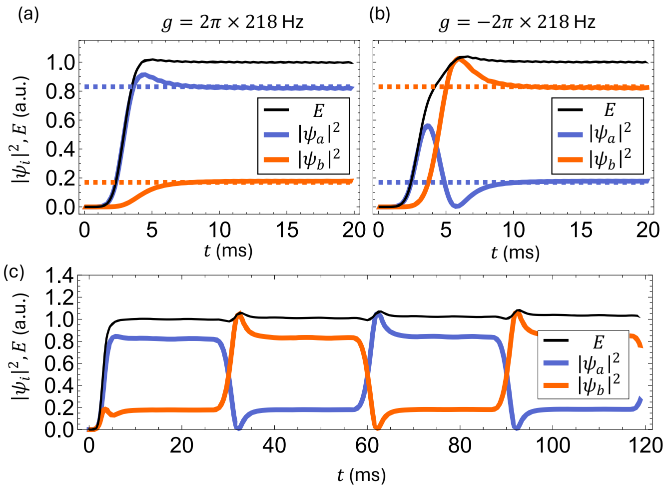


Fig. S5. Simulated nonlinear dynamics with an additional analog bandpass filter described by Eq. ($S6.3$), using the same gain parameters and cavity geometry as in Figs. 1(d,e) and 2(c) of the main text. The total energy $E$ is also shown to demonstrate the overshoot and oscillations of the total energy.

## S.7 Selection rule and perturbation theory for symmetry-forbidden transitions.

In the main text, we report a switching process between two dynamical attractors that is forbidden by symmetry in the absence of external perturbations. In this section, we formalize this observation using a symmetry-based selection rule and develop a perturbative framework to quantify how symmetry breaking enables the transition. For clarity, the analysis is carried out using the linearized effective Hamiltonian, which captures the relevant symmetry structure. To facilitate the discussion, we list all three eigenmodes before and after the transition in descending order of $\mathrm{Im}[\lambda]$.

**Before the transition:**

$$\begin{aligned}\psi_1 &= \{-1.47 - 2.03i, 1, 1\},\\ \psi_2 &= \{0.47 + 0.64i,1,1\},\\ \psi_3 &= \{0,1,-1\}.\end{aligned}$$

**After the transition:**

$$\begin{aligned}\psi_1' &= \{0,1,-1\},\\ \psi_2' &= \{0.47 - 0.64i,1,1\},\\ \psi_3' &= \{-1.47 + 2.03i, 1, 1\},\end{aligned}$$

where primes denote post-transition eigenmodes.

When the gain parameters satisfy $\mathrm{g_b} = \mathrm{g_c}$, the effective Hamiltonian possesses a discrete parity symmetry generated by the operator

$$\mathrm{P} = \begin{pmatrix} 1 & 0 & 0 \\ 0 & 0 & 1 \\ 0 & 1 & 0 \end{pmatrix},$$

which satisfies $[H_{\mathrm{eff}}, \mathrm{P}] = 0$ and $\mathrm{P}^2 = \mathrm{I}$.

The transition amplitude from a starting state $|\psi_1\rangle$ at time $\mathrm{t} = 0$ to a target mode $|\psi_1'\rangle$ at time $T$ is formally given by

$$\tau_{\mathrm{oe}} = \left|\left\langle \psi_1' \middle| \mathcal{T} \exp\left(-i\int_0^T H_{\mathrm{eff}}\, dt\right) \middle| \psi_1 \right\rangle\right|^2$$

where $H_{\mathrm{eff}}$ is the linearized Hamiltonian and $\mathcal{T}$ represent the time-ordering product. Since the attractors have different symmetry,

$$P|\psi_1\rangle = |\psi_1\rangle, \qquad P|\psi_1'\rangle = -|\psi_1'\rangle,$$

we obtain

$$\tau_{\mathrm{oe}} = \frac{1}{4}\left|\left\langle \psi_1' \middle| \left[\mathcal{T} \exp\left(-i\int_0^T H_{\mathrm{eff}}\, dt\right), P\right] \middle| \psi_1 \right\rangle\right|^2$$

Since $[H_{\mathrm{eff}}, \mathrm{P}] = 0$, the time-ordered propagator likewise commutes with $P$, as the symmetry operator commutes with each term in the Dyson expansion. Consequently, the transition amplitude vanishes, $\tau_{oe} = 0$.

In other words, since the two attractors have different parity, the transition between them is strictly forbidden when parity symmetry is preserved. However, transitions toward the eigenmode with the second-largest $\mathrm{Im}[\lambda]$ are allowed because they share the same parity, hence the system temporarily settles at the intermediate state $\psi_2' = \{0.47 - 0.64i, 1, 1\}$ in Fig. 4(a).

To enable the forbidden transition, parity symmetry must be explicitly broken. As implemented in the main text, this is achieved by introducing a small gain imbalance such that $g_b \neq g_c$. To quantify the effectiveness of this perturbation, we decompose the linearized Hamiltonian

$$H_{\text{eff}} = H_{\text{sym}} + V,$$

where

$$H_{\text{sym}} = \begin{pmatrix} \mathrm{i}g_{\mathrm{a}} & -\kappa/2 & -\kappa/2 \\ -\kappa/2 & \mathrm{i}\bar{g} & -\kappa/2 \\ -\kappa/2 & -\kappa/2 & \mathrm{i}\bar{g} \end{pmatrix}, \qquad \mathrm{V} = i\Delta g(t) \begin{pmatrix} 0 & 0 & 0 \\ 0 & 1 & 0 \\ 0 & 0 & -1 \end{pmatrix} = i\Delta g(t) V_0.$$

Here $\bar{g} = (g_b + g_c)/2$ and $\Delta g = (g_b - g_c)/2$. The unperturbed Hamiltonian $H_{\text{sym}}$ preserves parity symmetry, $[H_{\text{sym}}, P] = 0$, whereas the perturbation $V$ explicitly breaks it. Assuming the evolution time is short, the transition amplitude can be approximated by:

$$\begin{aligned} \tau_{\text{oe}} &\cong \frac{1}{4}\left|\left\langle \psi_1' \left| \left[ 1 - \int_0^T H_{\text{eff}}\, dt\, , P \right] \right| \psi_1 \right\rangle\right|^2 \\ &= \frac{1}{4}\left|\left\langle \psi_1' \left| \left[ \int_0^T V\, dt\, , P \right] \right| \psi_1 \right\rangle\right|^2 \\ &= \left| \int_0^T \langle \psi_1' | V | \psi_1 \rangle dt \right|^2 \\ &= \left| \int_0^T \Delta g(t) dt \right|^2 |\langle \psi_1' | V_0 | \psi_1 \rangle|^2 \end{aligned}$$

Therefore, the transition probability is determined by both the perturbation strength and the temporal profile of $\Delta g(t)$. Following the transient symmetry-breaking event, the system relaxes toward the new attractor. The relative amplitudes evolve as

$$\frac{a_i'(t+T)}{a_j'(t+T)} = \frac{a_i'(T)}{a_j'(T)} e^{-i(\lambda_i' - \lambda_j')t},$$

where the $|a_1'(T)| \propto \sqrt{\tau_{\text{att}}}$. The time $T_{\text{eq}}$ required for the target mode to become dominant can therefore be estimated by imposing $|a_1'(T_{\text{eq}})/a_2'(T_{\text{eq}})| = 1$, which yields the scaling

$$\Rightarrow T_{\text{eq}} - T \propto \log \frac{1}{a_1'(T)} \propto -\log \tau_{\text{oe}}.$$

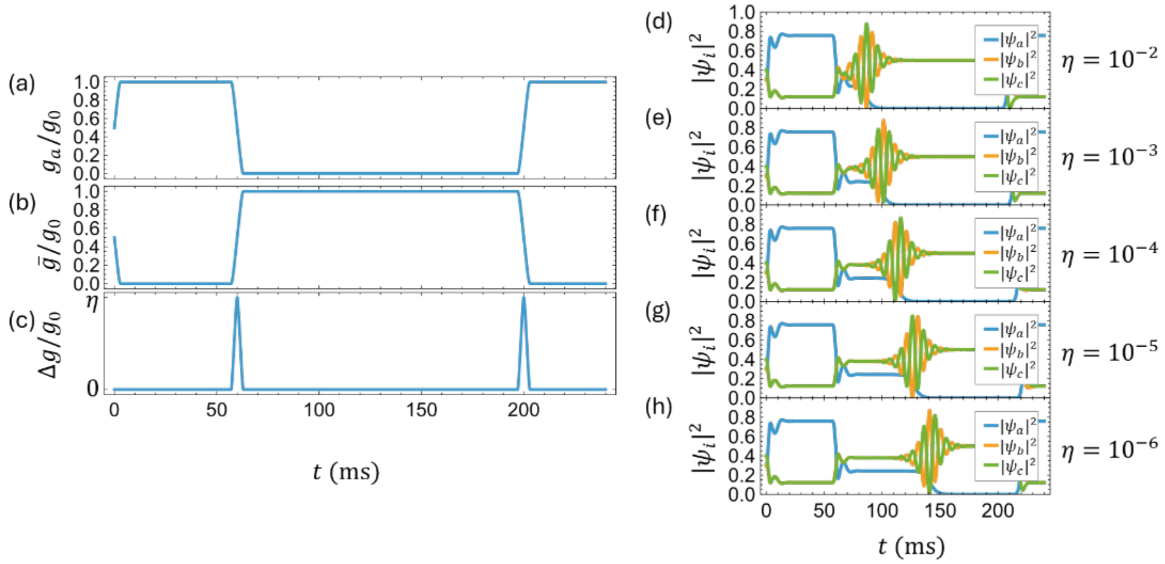


Figure S6 (a-c) Time signature of the gain coefficient $g_a, \bar{g}$ and $\Delta g$ where $\Delta g = \eta g_0 f(t)$ for a fixed $f(t)$, (d-h) Numerical simulation on with the nonlinear Hamiltonian with gain in (a-c), $\kappa = 163 \times 2\pi$ Hz and gain constant $g_0 = 218 \times 2\pi$ Hz. Each panel show a different perturbation strength form $\eta = 10^{-2}$ to $10^{-6}$. The converging speed show a dependent on $\eta$ with $-\log \eta$.

To verify this scaling behavior, we numerically solve the full nonlinear Schrödinger equation [Eq. (5) in the main text] with following gain parameters $g_a, g_b, g_c$ is now given by

$$g_a = g_a$$
$$g_b = \bar{g} + \frac{1}{2}\Delta g$$
$$g_c = \bar{g} - \frac{1}{2}\Delta g$$

where $g_a$, unperturbed gain $\bar{g}$ and perturbation $\Delta g = \eta g_0 f(t)$ is shown in Fig. S6. The transient symmetry-breaking modulation is applied at $t = 60$ ms, and the time signature of $\Delta g$ is kept fixed while the perturbation strength $\eta$ is varied. In this case:

$$\tau_{\mathrm{oe}} = \left| \int_0^T \Delta g(t) dt \right|^2 |\langle \psi_1' | V_0 | \psi_1 \rangle|^2 \propto \eta^2,$$
$$T_{eq} - T \propto -\log \tau_{oe} \propto -\log \eta$$

Figures S6 (d–h) show the resulting dynamics for perturbation strengths ranging from $\eta = 10^{-2}$ to $10^{-6}$. As $\eta$ decreases, the convergence time increases in accordance with the logarithmic scaling $T_{eq} - T \propto -\log \eta$, confirming the perturbative prediction. Finally, although the transient is not strictly short relative to the intrinsic dynamical timescale, we observe that the logarithmic scaling persists beyond the short time perturbative regime.

## S.8 Constructive parameter selection for target eigenmodes.

In this section we present a constructive parameter-selection method for designing a prescribed eigenmode of the linearized effective Hamiltonian $H_{\text{eff}}$ in an $n$-cavity network. This provides a practical way to treat the off-diagonal couplings as free design variables, while determining the diagonal detuning/gain terms accordingly. For clarity, we present the three-cavity case; the same construction extends directly to an $n$-cavity network by applying the same elementwise relation component by component.

Consider three inhomogeneous coupled cavities described by

$$H_{\text{eff}} = \begin{pmatrix} \delta\omega_a + ig_a & -\kappa_{ab} & -\kappa_{ac} \\ -\kappa_{ab} & \delta\omega_b + ig_b & -\kappa_{bc} \\ -\kappa_{ac} & -\kappa_{bc} & \delta\omega_c + ig_c \end{pmatrix}$$

Let $\psi = \{\psi_a, \psi_b, \psi_c\}$ be a target eigenvector and $\lambda$the desired eigenvalue. Enforcing $H_{\text{eff}}\psi = \lambda\psi$ yields the componentwise conditions

$$\delta\omega_i + ig_i = \lambda - \frac{(H_{\text{off}}\psi)_i}{\psi_i}, \qquad i \in \{a, b, c\}$$

For $\psi_i \neq 0$. where $H_{\text{off}}$ denotes the off-diagonal coupling matrix:

$$H_{\text{off}} = \begin{pmatrix} 0 & -\kappa_{ab} & -\kappa_{ac} \\ -\kappa_{ab} & 0 & -\kappa_{bc} \\ -\kappa_{ac} & -\kappa_{bc} & 0 \end{pmatrix}.$$

As a numerical illustration, fixing the target eigenvector $\psi = \{i, 2,4\}$ and select the couplings $\{\kappa_{ab}, \kappa_{ac}, \kappa_{bc}\} = \{-1,1,2\}$. Applying the above relation with $\lambda = 0$ gives

$$\begin{pmatrix} \delta\omega_a + ig_a \\ \delta\omega_b + ig_b \\ \delta\omega_c + ig_c \end{pmatrix} = \begin{pmatrix} -2i \\ 4 - i/2 \\ 1 + i/4 \end{pmatrix}$$

for which $\psi$ is exactly an eigenmode of $H_{\text{eff}}$. This example illustrates how the diagonal detuning/gain terms can be determined once the couplings and a target modal profile are specified. The construction generalizes straightforwardly to $n$ coupled cavities by applying the same componentwise relation. Given the enlarged parameter space, suitable choices of couplings and gain–loss are often available that can make the engineered eigenmode attracting, although we do not attempt a systematic search here.


1 R. N. Bracewell, *The Fourier Transform and Its Applications*. London: McGraw-Hill, 1965.
2 M. Rupin, G. Lerosey, J. d. Rosny and F. Lemoult, *New J. Phys.,* 2019, **21**, 093012.
3 C. Cho, X. Wen, N. Park and J. Li, *Nat. Comm.*, 2020, **11**, 251.